

A Magnetostatic Grad-Rubin Code for Coronal Magnetic Field Extrapolations

S.A. Gilchrist¹ · M.S. Wheatland¹

Received: 22 Apr 2012 / Accepted: 18 Sep 2012 / Published online: ●●●●●●●●

Abstract The coronal magnetic field cannot be directly observed, but in principle it can be reconstructed from the comparatively well observed photospheric magnetic field. A popular approach uses a nonlinear force-free model. Non-magnetic forces at the photosphere are significant meaning the photospheric data are inconsistent with the force-free model, and this causes problems with the modeling (De Rosa *et al.*, *Astrophys. J.* **696**, 1780, 2009). In this paper we present a numerical implementation of the Grad-Rubin method for reconstructing the coronal magnetic field using a magnetostatic model. This model includes a pressure force and a non-zero magnetic Lorentz force. We demonstrate our implementation on a simple analytic test case and obtain the speed and numerical error scaling as a function of the grid size.

S.A. Gilchrist · M.S. Wheatland
Sydney Institute for Astronomy, School of Physics, The University of
Sydney, NSW 2006, Australia
e-mail: s.gilchrist@physics.usyd.edu.au

1. Introduction

The solar magnetic field is observed primarily through its effect on the polarization of particular Zeeman sensitive spectral lines (Landi Degl’Innocenti and Landolfi, 2004). Observations of the Fe I multiplet provide two-dimensional maps of the vector magnetic field (vector magnetograms) close to the height of the photosphere. Unlike the photosphere, the corona lacks suitable magnetic lines and the coronal magnetic field cannot be determined except under exceptional circumstances (*e.g.* Hyder 1964), although new methods based on radio and infrared observations are presently being developed (*e.g.* White and Kundu 1997; Lin, Kuhn, and Coulter 2004). The inability to observe the coronal field presents a barrier to understanding important coronal magnetic phenomena, including solar flares.

In principle, the coronal magnetic field can be reconstructed from photospheric magnetograms by using a time-independent magneto-hydrodynamic model of the corona. The model requires solution of equations for the coronal magnetic field, \mathbf{B} , subject to boundary conditions derived from vector magnetogram data. The field obtained by solving the model is a proxy for observational data. How accurately the model field reflects the true coronal field depends on the quality of the magnetogram data, and the accuracy of the assumptions in the model.

Non-magnetic forces in the corona are generally negligible (Metcalf *et al.*, 1995; Gary, 2001) and this motivates coronal magnetic field reconstructions based on a force-free model, *i.e.* one in which only the magnetic (Lorentz) force is considered. In the force-free model the local current density is proportional to the magnetic field (Priest, 1984), with the proportionality factor α in general a function of position. The special case where α is independent of position is called a linear force-free field. The linear force-free model can be solved analytically and has been extensively studied (*e.g.* Nakagawa and Raadu 1972; Barbosa 1978; Seehafer 1978; Alissandrakis 1981). However the linear force-free model is of limited use as a model of the coronal magnetic field because of specific unphysical features (*e.g.* a linear force-free field in an unbounded domain has infinite magnetic energy (Alissandrakis, 1981)).

The problems with the linear force-free model spur interest in the nonlinear force-free model, where α varies with position. The formal boundary value problem for force-free modeling can be stated in different ways depending on the choice of boundary conditions on the photosphere (different possible choices are discussed by Grad and Rubin (1958) and Aly and Amari (2007)). Some definitions use all three components of \mathbf{B} over the entire boundary, while others prescribe the normal component of the magnetic field $\mathbf{B} \cdot \hat{\mathbf{n}}$ and the distribution of α over a single polarity of $\mathbf{B} \cdot \hat{\mathbf{n}}$, *i.e.* where $\mathbf{B} \cdot \hat{\mathbf{n}} < 0$ or where $\mathbf{B} \cdot \hat{\mathbf{n}} > 0$. The latter has been shown to be a well-posed¹ formulation of the problem (in certain domains) for sufficiently small values of α , while the former is an over specification of the problem (Bineau, 1972; Boulmezaoud and Amari, 2000; Kaiser, Neudert, and von Wahl, 2000). In both cases the boundary value problem is nonlinear and in general requires a numerical treatment. A number of different numerical solution methods have been developed for different statements of the nonlinear force-free boundary value problem (see reviews by Sakurai (1989), or more recently Wiegmann (2008)). Aly and Amari (2007) review the different methods and the choice of boundary conditions used in each case.

Although appealing in its simplicity, the application of the (nonlinear) force-free model to magnetogram data has proved problematic (*e.g.* De Rosa *et al.* 2009; Schrijver *et al.* ■

¹A boundary value problem is said to be well-posed if it has a unique solution which depends continuously on the boundary conditions.

2008). The numerical solution methods are generally iterative, and when applied to solar data the iterations may fail to converge (De Rosa *et al.*, 2009). The problem is particular pronounced when large electric currents are present in the data. (It should be noted that convergence problems were not reported by De Rosa *et al.* (2009) for two of the methods which are based on a well-posed formulation of the boundary value problem.)

A possible reason for the problems is that the data departs significantly from a force-free state (Gary, 2001; Metcalf *et al.*, 1995). This is expected to affect different solution methods in different ways. For methods using the well-posed formalism, two solutions are obtained for a single magnetogram corresponding to the two choices of polarity. In practice, these two solutions are qualitatively and quantitatively different due to the forced nature of the boundary data. For methods which over specify the problem the iterative methods can never converge to a force-free state if the boundary data are not consistent with the force-free model. In practice, this leads to numerical solutions with residual forces and nonzero divergence. A proposed solution to this problem is ‘preprocessing’ of the data (Wiegelmann, Inhester, and Sakurai, 2006; Fuhrmann, Seehafer, and Valori, 2007). With this technique the data are modified to be consistent with small net forces and torques in the overlying volume while maintaining minimal departure from the original data. However, the preprocessed data are not necessarily consistent with the force-free model (De Rosa *et al.*, 2009) and mixed results have been obtained in the modelling: in some cases the problems were reduced (Schrijver *et al.*, 2008) and in other cases there was no significant improvement (De Rosa *et al.*, 2009).

Another approach is to develop static models of the coronal magnetic field which incorporate non-magnetic forces, *i.e.* magneto-hydrostatic models, which incorporate gravity and gas pressure forces. The special case of a model with only magnetic and pressure forces may be called a magnetostatic model. This model requires the prescription of pressure as a boundary condition. Presently, the photospheric pressure distribution is difficult to obtain observationally compared to the magnetic field. This is a limitation of magnetostatic (and magneto-hydrodynamic) models in application to solar data.

A number of methods for solving the magneto-hydrostatic and magnetostatic equations have been developed for modeling the coronal magnetic field. The optimization procedure developed for the nonlinear force-free model has been extended to magneto-hydrostatic and magnetostatic models in Cartesian geometry (Wiegelmann and Inhester, 2003; Wiegelmann and Neukirch, 2006), and spherical geometry (Wiegelmann *et al.*, 2007). Amari, Boulbe, and Boulmezaoud (2009) presented a finite element implementation of the Grad-Rubin method (Grad and Rubin, 1958) for solving a magnetostatic model which is applicable in arbitrary geometry. In addition semi-analytic approaches have been developed but these provide only restricted, and not general, solutions (*e.g.* Rudenko 2001).

In this paper we present a numerical code to solve a general magnetostatic model of the coronal magnetic field of an active region. Our code is an implementation of the Grad-Rubin method (Grad and Rubin, 1958) to the magnetostatic equations in the half-space $z \geq 0$. The Grad-Rubin method has previously been used to solve the nonlinear force-free equations in the half-space for coronal reconstructions (*e.g.* Wheatland 2006; Amari, Boulmezaoud, and Mikic 1999), and to solve the magneto-static equations in toroidal geometry (Reiman and Greenside, 1986) and in arbitrary geometry (Amari, Boulbe, and Boulmezaoud, 2009). The Grad-Rubin method has the advantage of, in principle, solving the magnetostatic equations to the limited imposed by numerical accuracy (*e.g.* truncation error due to the finite grid size), assuming the

Grad-Rubin iteration procedure converges. We apply the code to a simple analytic test case as a demonstration, and to investigate the speed and numerical error scaling of the implementation. The resulting code and method does not yet provide a practical tool for coronal field modeling from solar data, because of the neglect of the gravity force, but it is a significant step in this direction.

This paper is structured as follows. Section 2 presents the magnetostatic equations, and the boundary value problem to be solved. Section 3 is a brief summary of the Grad-Rubin method, and describes our specific implementation of the method in code. Section 4 presents the analytic test case used. Section 5 presents the results, and Section 6 contains discussion of the results and the conclusion.

2. Magnetostatic Equations and Boundary Value Problem

2.1. The Model

The magneto-hydrostatic equations with the gravity force neglected are

$$\nabla \times \mathbf{B} = \mu_0 \mathbf{J}, \quad (1)$$

$$\nabla \cdot \mathbf{B} = 0, \quad (2)$$

and

$$\mathbf{J} \times \mathbf{B} - \nabla p = 0 \quad (3)$$

(Priest, 1984). Here p is the gas pressure, \mathbf{J} is the electric current density, and \mathbf{B} is the magnetic field vector.

2.2. The Boundary Value Problem

For a localized active region the curvature of the photosphere is small, so we solve Equations (1)-(3) in the half-space $z \geq 0$, with the $z = 0$ plane representing the photosphere. The appropriate boundary conditions prescribed on the $z = 0$ plane are B_z , together with p and J_z prescribed over a single polarity of the magnetic field, *i.e.* p and J_z are prescribed only at points with $B_z > 0$ or at points where $B_z < 0$ (Grad and Rubin, 1958). We denote the boundary values of the magnetic field, pressure and current density by B_{obs} , p_{obs} and J_{obs} respectively. These boundary conditions are believed to be the correct physical boundary conditions for the magnetostatic model.

Equations (1)-(3) are solved numerically in the finite volume

$$\Omega_b = \{(x, y, z) | 0 \leq x \leq L_x, 0 \leq y \leq L_y, 0 \leq z \leq L_z\}. \quad (4)$$

In addition to the $z = 0$ plane, Ω_b has five additional plane boundaries on which boundary conditions are required. Magnetogram data only provide boundary conditions on the $z = 0$ plane and reasonable assumptions must be made for the remaining five. This problem is faced by all reconstruction codes regardless of the particular model or method used, and models including more physics typically require more boundary conditions at each boundary.

We choose boundary conditions on the magnetic field such that all field lines are connected to the lower boundary at two points (*i.e.* there are no open field lines). The need for this is discussed in Section 3.2.1. We achieve this in practice by imposing either (i) closed boundary conditions on the top and side boundaries

$$\mathbf{B} \cdot \hat{\mathbf{n}} = 0, \quad (5)$$

where $\hat{\mathbf{n}}$ denotes the unit normal vector to each boundary, or (ii) a closed top boundary condition

$$\mathbf{B} \cdot \hat{\mathbf{z}} = 0, \quad (6)$$

together with periodic boundary conditions on the side boundaries. For the periodic case any field line which leaves the computational volume by a side boundary re-enters on the opposite side, and therefore eventually connects to the lower boundary. These boundary conditions specify that magnetic flux only enters and leaves through the lower boundary, which requires that the lower boundary is flux balanced.

3. Numerical Implementation of the Grad-Rubin Method

In this section we outline our implementation of the Grad-Rubin method in code. The approach is similar to that for the force-free code described in Wheatland (2007).

3.1. The Grad-Rubin Method

The Grad-Rubin method (also called the current-field iteration method) is an iterative scheme for solving the magnetostatic equations (Grad and Rubin, 1958). In this method the nonlinear equations (Equations (1)-(3)) are replaced with a set of linear equations which are solved at each iteration.

Here we briefly outline a single Grad-Rubin iteration (a more detailed description is given by Grad and Rubin (1958)). We denote a quantity after k Grad-Rubin iterations using a superscript, so for example $\mathbf{B}^{(k)}$ denotes the magnetic field in our computational volume after k iterations starting from an initial magnetic field $\mathbf{B}^{(0)}$. In practice the iteration is initiated with a potential field in the volume calculated from B_{obs} , which we denote as $\mathbf{B}^{(0)} = \mathbf{B}_0$. In the following we assume $\mathbf{B}^{(k)}$ is known from a previous iteration, or is the initial potential field. A single iteration consists of the following steps.

1. Calculate a new pressure $p^{(k+1)}$ in the volume by solving

$$\mathbf{B}^{(k)} \cdot \nabla p^{(k+1)} = 0, \quad (7)$$

with boundary conditions

$$p^{(k+1)}|_{z=0} = p_{\text{obs}} \quad (8)$$

prescribed over one polarity of B_{obs} .

2. Calculate the component of the current density perpendicular to the magnetic field in the volume using

$$\mathbf{J}_{\perp}^{(k+1)} = \nabla p^{(k+1)} \times \mathbf{B}^{(k)} / |\mathbf{B}^{(k)}|^2. \quad (9)$$

3. Calculate the component $\mathbf{J}_{\parallel}^{(k+1)}$ of the current density parallel to the magnetic field in the volume. The parallel component can be written as

$$\mathbf{J}_{\parallel}^{(k+1)} = \sigma^{(k+1)} \mathbf{B}^{(k)} / \mu_0, \quad (10)$$

where $\sigma^{(k+1)}$ is a scalar function of position. The parameter $\sigma^{(k+1)}$ is calculated in the volume by solving (Grad and Rubin, 1958)

$$\nabla \sigma^{(k+1)} \cdot \mathbf{B}^{(k)} = -\mu_0 \nabla \cdot \mathbf{J}_{\perp}^{(k+1)}, \quad (11)$$

with boundary conditions

$$\sigma|_{z=0} = \sigma_{\text{obs}}^{(k+1)} \quad (12)$$

where

$$\sigma_{\text{obs}}^{(k+1)} = \left. \frac{\mu_0 (\mathbf{J}_{\perp}^{(k+1)} \cdot \hat{\mathbf{z}} - J_{\text{obs}})}{B_{\text{obs}}} \right|_{z=0}. \quad (13)$$

The boundary conditions $\sigma_{\text{obs}}^{(k+1)}$ are prescribed over a single polarity of B_{obs} and are calculated using Equation (13) at each iteration. The form of Equation (13) is

such that $\mathbf{J}^{(k+1)} \cdot \hat{\mathbf{z}} = J_{\text{obs}}$ on the lower boundary (over the polarity of B_{obs} chosen for the boundary conditions).

Equations (9)-(10) define the total current density in the volume:

$$\mathbf{J}^{(k+1)} = \mathbf{J}_{\perp}^{(k+1)} + \sigma^{(k+1)} \mathbf{B}^{(k)} / \mu_0. \quad (14)$$

4. Calculate the new magnetic field in the volume by solving Ampere's law

$$\nabla \times \mathbf{B}^{(k+1)} = \mu_0 \mathbf{J}^{(k+1)}, \quad (15)$$

where the boundary conditions on $\mathbf{B}^{(k+1)}$ are those in Section 2.

3.2. Overview of the Code

The code solves the magnetostatic equations in the finite Cartesian domain Ω_b using the Grad-Rubin method. The numerical grid is uniformly spaced with N grid points along each dimension, so there are N^3 grid points in total, and in the following we write $L = L_x = L_y = L_z$ for simplicity. The grid spacing is $L/(N-1)$, and the coordinates of the grid points are $(x_i, y_j, z_k) = (i, j, k)L/(N-1)$, where $0 \leq i, j, k \leq N-1$.

In the following we describe the implementation of the Grad-Rubin steps identified in Section 3.1 in detail, identifying some of the numerical methods used. The code is an implementation in FORTRAN90 using double precision floating point numbers (Press *et al.*, 1992). The code is parallelized for shared memory multiprocessors using OpenMP (Chandra *et al.*, 1990).

3.2.1. Step 1: Update of Pressure in the Volume

Equation (7) is solved by a field line tracing (or characteristic) method. The same method is used in some existing force-free Grad-Rubin method implementations for solving $\mathbf{B} \cdot \nabla \alpha = 0$ (*e.g.* Amari, Boulmezaoud, and Mikic 1999; Wheatland 2006, 2007), where α is the force-free parameter defined by $\nabla \times \mathbf{B} = \alpha \mathbf{B}$. Equation (7) has also been solved using a finite element method (Amari, Boulmezaoud, and Aly, 2006). In the force-free case the tracing is used to update α in the volume, and here it is used to update the pressure.

The procedure is as follows. For each grid point (x_i, y_j, z_k) the field line threading (x_i, y_j, z_k) is traced to the point (x_0, y_0) where it crosses the lower boundary with the appropriate polarity for the boundary conditions. The pressure at the grid point is then assigned to be equal to the boundary value:

$$p(x_i, y_j, z_k) = p_{\text{obs}}(x_0, y_0). \quad (16)$$

This procedure solves Equation (7) because the pressure is constant along a magnetic field line. The tracing is performed in either the forward or backward direction along the field line, with the direction chosen such that the point (x_0, y_0) has the appropriate polarity for B_{obs} . Fourth order Runge-Kutta is used for the numerical tracing (Press *et al.*, 1992). Because the path of the field line is not confined to grid points, trilinear interpolation is used to estimate \mathbf{B} between grid points (Press *et al.*, 1992). Similarly, bilinear interpolation is used to compute p_{obs} at the boundary point (x_0, y_0) , which also may not coincide with a grid point.

Open field lines (see Section 2.2) would present a problem for this method. Since p_{obs} is only prescribed over a single polarity, it would be impossible to assign pressure to points threaded by field lines which connect to the lower boundary at only one polarity,

opposite to that for which p_{obs} is prescribed. We avoid this problem by preventing open field lines through the choice of boundary conditions on \mathbf{B} explained in Section 2.2. This eliminates the problem but introduces artificial boundary conditions on the top and side boundaries. However, the region of interest can be isolated from the effects of the boundaries by using a large domain.

3.2.2. Steps 2 and 3: Update of the Current Density in the Volume

Given the updated values $p^{(k+1)}$ for the pressure in the volume, Equation (9) may be directly evaluated at every gridpoint to give the perpendicular current \mathbf{J}_{\perp} in the volume. The derivatives in the gradient on the right hand side are evaluated numerically using a centered difference approximation (Press *et al.*, 1992).

A particular problem is encountered with the evaluation of the perpendicular current \mathbf{J}_{\perp} in the volume at each iteration (step 2 in the enumeration of the procedure in Section 3.1), for the test cases considered here. The perpendicular current is calculated using Equation (9):

$$\mathbf{J}_{\perp}^{(k+1)} = \nabla p^{(k+1)} \times \mathbf{B}^{(k)} / |\mathbf{B}^{(k)}|^2. \quad (17)$$

For the analytic solutions we use in Section 5 there are locations in the volume where $\mathbf{B} = 0$ and \mathbf{J}_{\perp} is finite. The perpendicular current is not correctly evaluated numerically at these points. To prevent this we choose grid sizes for our problems such that the points with $\mathbf{B} = 0$ fall between grid points. This removes the problem, which is due to the artificial nature of the test cases.

The value of $\sigma^{(k+1)}$ at each gridpoint is then obtained by solving Equation (11). This equation may be integrated along a field line to give the formal solution

$$\sigma^{(k+1)}(x_i, y_j, z_k) = \sigma_{\text{obs}}(x_0, y_0) - \gamma \int_0^{s_0} \nabla \cdot \mathbf{J}_{\perp}^{(k+1)}(\mathbf{x}(s)) / |\mathbf{B}^{(k)}(\mathbf{x}(s))| ds, \quad (18)$$

where

$$\gamma = \begin{cases} +1 & \text{if } J_{\text{obs}} \text{ is prescribed over } B_z > 0 \\ -1 & \text{if } J_{\text{obs}} \text{ is prescribed over } B_z < 0, \end{cases} \quad (19)$$

where $\mathbf{x}(s)$ is the path of the field line (the parameter s is the arc length along the field line), and where $\mathbf{x}(s_0)$ is the point $(x_0, y_0, 0)$ at which the boundary conditions on $\sigma^{(k+1)}$ are imposed. Trilinear interpolation is used to assign values in the argument of the integral along a field line, and the integral is evaluated using the trapezoidal rule (Press *et al.*, 1992).

The field line tracing needed for steps one and two (updating pressure and σ) is the computationally slow part of this implementation of the Grad-Rubin method. The number of operations for the field line tracing scales as N^4 for a grid with N^3 points (Wheatland, 2006). In the following we will write ‘ $\sim N^4$ ’ to denote such a scaling. The code parallelizes the process using OpenMP, with the workload divided such that different code threads trace different field lines.

It is important to understand the accuracy of the numerical solutions for $p^{(k)}$ and $\sigma^{(k)}$. For the field line tracing solution we can infer an approximate scaling for the numerical error as follows. Trilinear interpolation has truncation error $\sim 1/N^2$ (Zikanov, 2010), and on average a field line requires $\sim N$ Runge-Kutta steps to reach the lower boundary. Therefore the total numerical error introduced by tracing a field line to the lower boundary has scaling $\sim N \times 1/N^2 = 1/N$. We expect this error to be the dominant error in the calculation, and so the error scaling for the whole computation is $\sim 1/N$. This error scaling has been confirmed for the force-free case (Wheatland, 2006).

3.2.3. Step 4: Update of the Magnetic Field in the Volume

The magnetic field may be expressed as $\mathbf{B}^{(k)} = \mathbf{B}_0 + \mathbf{B}_c^{(k)}$, where \mathbf{B}_0 is the potential field satisfying $\nabla \times \mathbf{B}_0 = 0$ together with the boundary condition

$$\mathbf{B}_0 \cdot \hat{\mathbf{z}}|_{z=0} = B_{\text{obs}}, \quad (20)$$

and where $\mathbf{B}_c^{(k)}$ is a current carrying field satisfying $\nabla \times \mathbf{B}_c^{(k)} = \mu_0 \mathbf{J}^{(k)}$ together with the homogeneous boundary condition

$$\mathbf{B}_c^{(k)} \cdot \hat{\mathbf{z}}|_{z=0} = 0. \quad (21)$$

The fields $\mathbf{B}_c^{(k)}$ and \mathbf{B}_0 have the same boundary conditions on the top and side boundaries (either closed boundary conditions on all other boundaries, or closed top boundary conditions and periodic side boundary conditions, as discussed in Section 2.2).

For the potential field a scalar potential ϕ can be introduced defined by

$$\nabla \phi = -\mathbf{B}_0, \quad (22)$$

and the problem reduces to solving Laplace's equation (Jackson, 1998):

$$\nabla^2 \phi = 0. \quad (23)$$

Laplace's equation has well-known Fourier solutions in Cartesian geometry (Morse and Feshbach, 1953), and we use a two-dimensional Fourier series solution with the expansion performed in the x and y directions. For periodic boundary conditions the components of our potential field are²

$$B_{0x}(x, y, z) = \sum_{m=0}^{\infty} \sum_{n=0}^{\infty} c_{mn} i k_m \cosh(k[z - L]) e^{i(xk_m + yk_n)}, \quad (24)$$

$$B_{0y}(x, y, z) = \sum_{m=0}^{\infty} \sum_{n=0}^{\infty} c_{mn} i k_n \cosh(k[z - L]) e^{i(xk_m + yk_n)}, \quad (25)$$

and

$$B_{0z}(x, y, z) = \sum_{m=0}^{\infty} \sum_{n=0}^{\infty} c_{mn} k \sinh(k[z - L]) e^{i(xk_m + yk_n)}. \quad (26)$$

where $k_m = 2\pi m/L$, $k_n = 2\pi n/L$ and $k^2 = k_m^2 + k_n^2$. The Fourier series coefficients are derived from the boundary conditions:

$$c_{mn} = -\frac{1}{L^2} \int_0^L \int_0^L dx dy B_{\text{obs}}(x, y) e^{-i(xk_m + yk_n)} / \sinh(kL). \quad (27)$$

As explained in Section 2.2, we also use a solution with closed boundaries, and the expression for the components of this field are similar (see Appendix A). Equations (24)-(25) can be computed using Fast Fourier transforms, in which case $\sim N^3 \log(N)$

²We note that this solution is a special case of the linear force-free solution due to Barbosa (1978), and is obtained by setting $\alpha = 0$ in that solution.

operations are required to evaluate the potential field for a grid of N^3 grid points (Press *et al.*, 1992). This makes step 4 relatively fast, computationally.

For the non-potential component \mathbf{B}_c we use a three-dimensional Fourier series solution to the vector Poisson equation, working with a vector potential \mathbf{A}_c such that $\mathbf{B}_c = \nabla \times \mathbf{A}_c$ (Morse and Feshbach, 1953). The components of the field are

$$B_{cx}(x, y, z) = \sum_{m=0}^{\infty} \sum_{n=0}^{\infty} \sum_{p=0}^{\infty} \left[k_n i a_{mnp}^{(3)} - k_p a_{mnp}^{(2)} \right] \cos(k_p z) e^{i(k_m x + k_n y)} / k^2, \quad (28)$$

$$B_{cy}(x, y, z) = \sum_{m=0}^{\infty} \sum_{n=0}^{\infty} \sum_{p=0}^{\infty} \left[k_p a_{mnp}^{(1)} - k_m i a_{mnp}^{(3)} \right] \cos(k_p z) e^{i(k_m x + k_n y)} / k^2, \quad (29)$$

$$(30)$$

and

$$B_{cz}(x, y, z) = \sum_{m=0}^{\infty} \sum_{n=0}^{\infty} \sum_{p=0}^{\infty} i \left[k_m a_{mnp}^{(2)} - k_n a_{mnp}^{(1)} \right] \sin(k_p z) e^{i(k_m x + k_n y)} / k^2. \quad (31)$$

Here $k_m = 2\pi m/L$, $k_n = 2\pi n/L$, and $k_p = \pi p/L$. The coefficients $a_{mnp}^{(i)}$, with $i = 1, 2, 3$ are given by:

$$a_{mnp}^{(1)} = \frac{2\mu_0}{L^3} \int_0^L \int_0^L \int_0^L J_x(x, y, z) e^{-i(k_m x + k_n y)} \sin(k_p z) dx dy dz, \quad (32)$$

$$a_{mnp}^{(2)} = \frac{2\mu_0}{L^3} \int_0^L \int_0^L \int_0^L J_y(x, y, z) e^{-i(k_m x + k_n y)} \sin(k_p z) dx dy dz, \quad (33)$$

and

$$a_{mnp}^{(3)} = \frac{2\mu_0}{L^3} \int_0^L \int_0^L \int_0^L J_z(x, y, z) e^{-i(k_m x + k_n y)} \cos(k_p z) dx dy dz. \quad (34)$$

The coefficients given by Equations (32)-(34), and the solution given by Equations (28)-(31), are computed in $\sim N^3 \log(N)$ operations using a combination of fast Fourier, fast sine, and fast cosine transforms (Poularikas, 1996). The corresponding solution for \mathbf{B}_c with closed side boundaries is given in Appendix B, which also provides more detail on how these solutions are derived.

4. Analytic Test Case

To test the code we use a simple analytic solution to the magnetostatic equations (Wiegelmann, 1998; Wiegelmann and Inhester, 2003) which is a generalization of a force-free field in Sturrock (1994), and which may be derived using the generating function method. The solution describes a sheared magnetic arcade with translational symmetry in the y direction and periodicity in the x direction.

For the problem at hand we modify the sheared arcade solution by imposing a closed top boundary condition (to match the boundary condition required by our Grad-Rubin method):

$$B_z(x, y, L) = 0. \quad (35)$$

The components of the resulting magnetostatic field are

$$B_x(x, z) = \psi_0 l \sin(kx) \cosh[l(L - z)], \quad (36)$$

$$B_y(x, z) = \psi_0 \lambda \sqrt{1 - a_0} \sin(kx) \sinh[l(L - z)], \quad (37)$$

and

$$B_z(x, z) = \psi_0 k \cos(kx) \sinh[l(L - z)], \quad (38)$$

and the pressure is given by

$$p(x, z) = \psi_0^2 \left(\frac{a_0 \lambda}{2\mu_0} \right) \sin^2(kx) \sinh^2[l(z - L)], \quad (39)$$

where k , λ , ψ_0 and a_0 are free parameters subject to $0 \leq a_0 \leq 1$ and $l = \sqrt{k^2 - \lambda^2}$.

The parameter λ determines the currents in the volume, with $\lambda = 0$ giving a potential field. The parameter a_0 sets the pressure in the volume, and the special case $a_0 = 0$ is a linear force-free field with force-free parameter $\alpha = \lambda$. The parameter a_0 may be used to enforce closed side boundary conditions in y with the choice $a_0 = 1$. The parameter k determines the period of the solution in the x direction, and the constant ψ_0 , which determines the magnitude of the field, is chosen to be

$$\psi_0 = \frac{1}{\sinh(L)k}, \quad (40)$$

to specify $\max(|B_{\text{obs}}|) = 1$ on the lower boundary.

The boundary conditions in the $z = 0$ plane with the choice of ψ_0 given by Equation (40) are

$$B_{\text{obs}} = \cos(kx), \quad (41)$$

$$p_{\text{obs}} = \frac{a_0 \lambda}{2\mu_0 k^2} \sin^2(kx), \quad (42)$$

and

$$J_{\text{obs}} = \mu_0 \lambda \sqrt{1 - a_0} \cos(kx). \quad (43)$$

A schematic diagram of the field lines of the solution is shown in Figure 1, for the choices $k = 2\pi/L$, $a_0 = 0.5$, and $\lambda = \pi/(2L)$. The view in the left panel of the Figure is along the y axis. This perspective shows the arcade-like field line structure. The right panel of Figure 1 shows a top-down view of the particular field lines shown as dashed

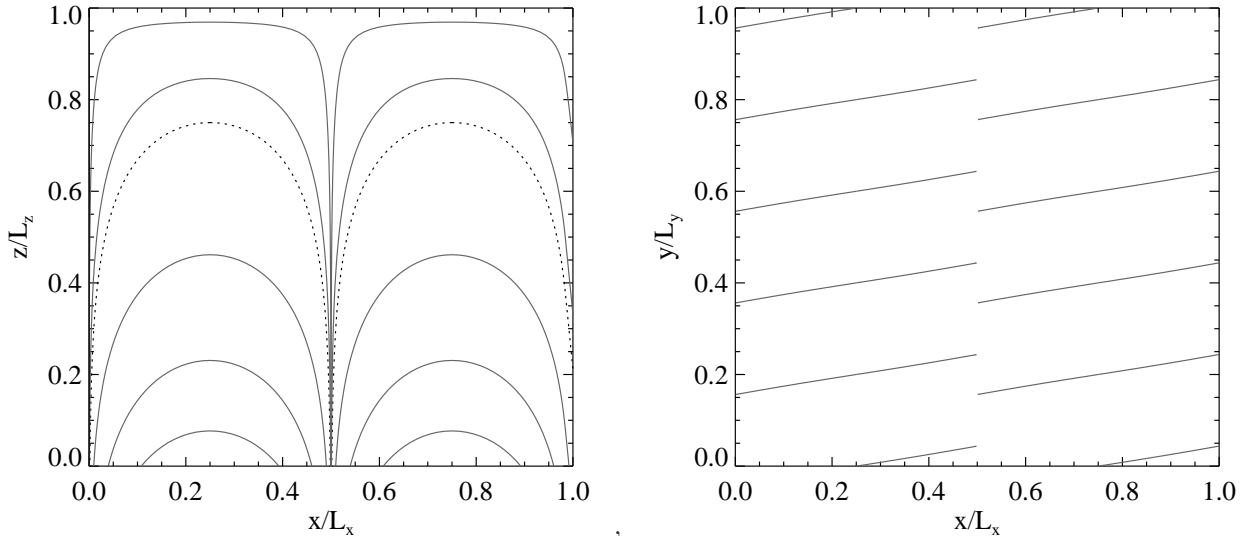


Figure 1. Field lines for the analytic magnetostatic field test case (see Section 4) with parameters $k = 2\pi/L$, $a_0 = 0.5$, and $\lambda = \pi/(2L)$. In the left panel the point of view is along the y axis. The right panel shows a top-down view of the field lines indicated by the dashed curves in the left panel. These field lines are sheared with respect to the x axis, at an angle of $\approx 10^\circ$.

curves shown in the left panel. The top of these field lines is at $z = 3L/4$. This perspective shows that the arcade is sheared. For the given solution the shear angle is $\approx 10^\circ$ for the field lines with the height shown.

5. Results

In this section we apply the code to the test case in Section 4 for two different choices of parameters. The first choice is for a calculation with periodic side boundary conditions, and the second is for a calculation with closed side boundary conditions. For both cases the tests are performed several times on grids of varying size. The convergence of the Grad-Rubin iteration is demonstrated, and the speed of the code as a function of problem size (introduced in Section 3.2.2) is confirmed. We also examine the accuracy of the numerical solution by comparison with the analytic solution, and investigate the accuracy as a function of grid size, for comparison with the estimate of the scaling of the accuracy given in Section 3.2.2.

5.1. Test Case with Periodic Side Boundaries

For the first test we use the parameters $k = 2\pi(1 - 1/N)/L$, $\lambda = \pi/(2L)$ and $a_0 = 0.5$. The parameter k is chosen to vary with N so that the periodicity of the solution matches the periodicity of the discrete Fourier transform (Press *et al.*, 1992). A side effect of this is that the test case differs between grid sizes. In particular the boundary conditions, which depend on k through Equations (41)-(43), are different. However, for large N the difference is small. We apply the code to the test case with three different grid sizes ($N = 51, 101, 151$), and in each case we perform 30 Grad-Rubin iterations starting from a potential field.

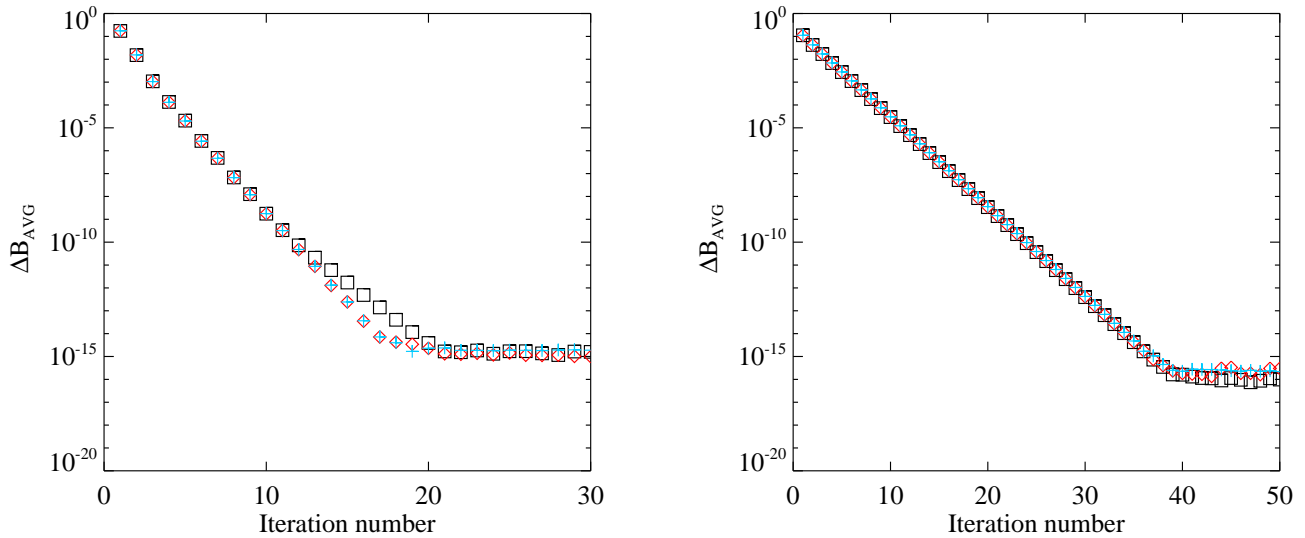


Figure 2. The mean absolute change in the field ΔB_{avg} as a function of iteration number for the application of the Grad-Rubin method to the test cases. The left panel shows ΔB_{avg} for the three tests with periodic side boundary conditions, and the right panel shows ΔB_{avg} for the three tests with closed boundary conditions. The different symbols represent ΔB_{avg} for different grid sizes N . In both panels the $N = 65$ case is shown with squares, the $N = 101$ case is shown with diamonds, and the $N = 151$ case is shown with plus signs, and the scale on the y axis is logarithmic.

The convergence of the Grad-Rubin iteration is measured by the absolute change in the field at each iteration, *i.e.*

$$\Delta B_{\text{avg}} = \langle |\mathbf{B}^{(k)} - \mathbf{B}^{(k-1)}| \rangle \quad (44)$$

where $\langle \rangle$ denotes the average over all points in the computational volume. The left panel of Figure 2 shows ΔB_{avg} over 30 Grad-Rubin iterations for the three different grid sizes. The squares show the case with $N = 65$, the diamonds show the case with $N = 101$, and the plus signs show the case with $N = 151$. In all three cases the Grad-Rubin iteration converges: ΔB_{avg} decreases exponentially for ≈ 15 iterations before becoming approximately constant. The rate of convergence does not appear to depend strongly on grid size.

The numerical solution after 30 iterations is compared to the analytic solution. This is done qualitatively by comparing the field lines of the analytic solution, the initial potential field, and the numerical solution. The left panel of Figure 3 shows the field lines of the analytic solution (red field lines), and the field lines of the potential field (blue field lines) viewed looking down on the computational domain. There is a significant difference between the two sets of field lines. The right panel of Figure 3 shows the field lines of the analytic solution (red field lines), and the field lines of the numerical solution after 30 Grad-Rubin iterations (blue field lines) from the same viewpoint. The two sets of field lines closely coincide, confirming that the Grad-Rubin iteration has converged to the analytic solution.

In addition to this qualitative comparisons, we compare the analytic and numerical solutions quantitatively. Several metrics have been developed for this purpose in the context of nonlinear force-free modeling (Schrijver *et al.*, 2006). The various metrics show similar results, so for brevity we present only the mean vector error

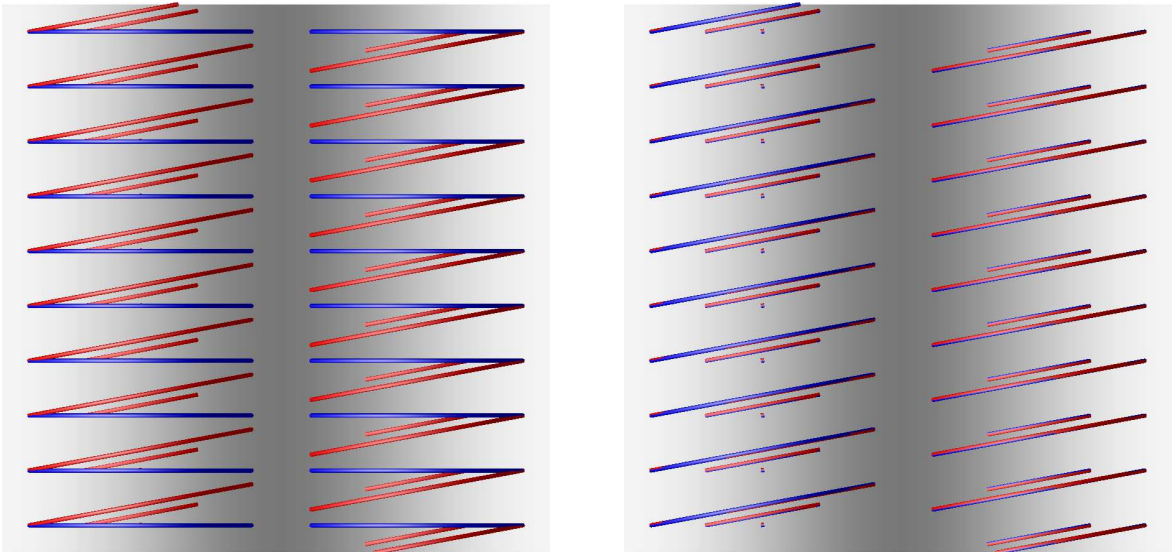


Figure 3. Comparisons between the field lines for the analytic solution, the Grad-Rubin solution and the initial potential field for the test case calculation in Section 5.1. The left panel shows the analytic solution (red field lines) and the potential field (blue field lines). The right panel shows the analytic solution (red field lines) and the numerical solution after 30 Grad-Rubin iterations (blue field lines). The solutions are viewed looking down from the top of the computational domain. The $z = 0$ plane is shaded to show B_{obs} (regions with $B_{\text{obs}} < 0$ are dark and those with $B_{\text{obs}} > 0$ are light). The solution after 30 Grad-Rubin iterations closely matches the analytic solution.

$$E_m = \left\langle \frac{|\mathbf{B} - \mathbf{b}|}{|\mathbf{B}|} \right\rangle, \quad (45)$$

and the metric

$$E_{\text{CS}} = 1 - \left\langle \frac{\mathbf{B} \cdot \mathbf{b}}{|\mathbf{B}| |\mathbf{b}|} \right\rangle, \quad (46)$$

which is based on the Cauchy-Schwartz inequality³. In both these definitions the analytic solution is \mathbf{B} , the numerical solution is \mathbf{b} , and the average is over all grid points in the domain. For two exactly matching fields $E_m = 0$ and $E_{\text{CS}} = 0$. The mean vector error is a measure of the difference between the magnitude and direction of \mathbf{B} and \mathbf{b} at each grid point, while E_{CS} is only sensitive to the differences in the direction of the fields.

We also compute

$$E_{\text{div}} = \langle |\nabla \cdot \mathbf{b}| \rangle, \quad (47)$$

which is a measure of the divergence of the numerical solution \mathbf{b} . A second-order finite difference approximation is used to compute the divergence at each grid point (Press *et al.*, 1992). In principle E_{div} should be zero, but this is not achieved in practice due to the finite numerical accuracy of the solution, and the truncation error introduced by the numerical approximation to differentiation. The truncation error in the derivative has a scaling $\sim 1/N^2$ (Press *et al.*, 1992).

³These metrics are chosen because they show the largest discrepancy between the numerical and the analytic fields.

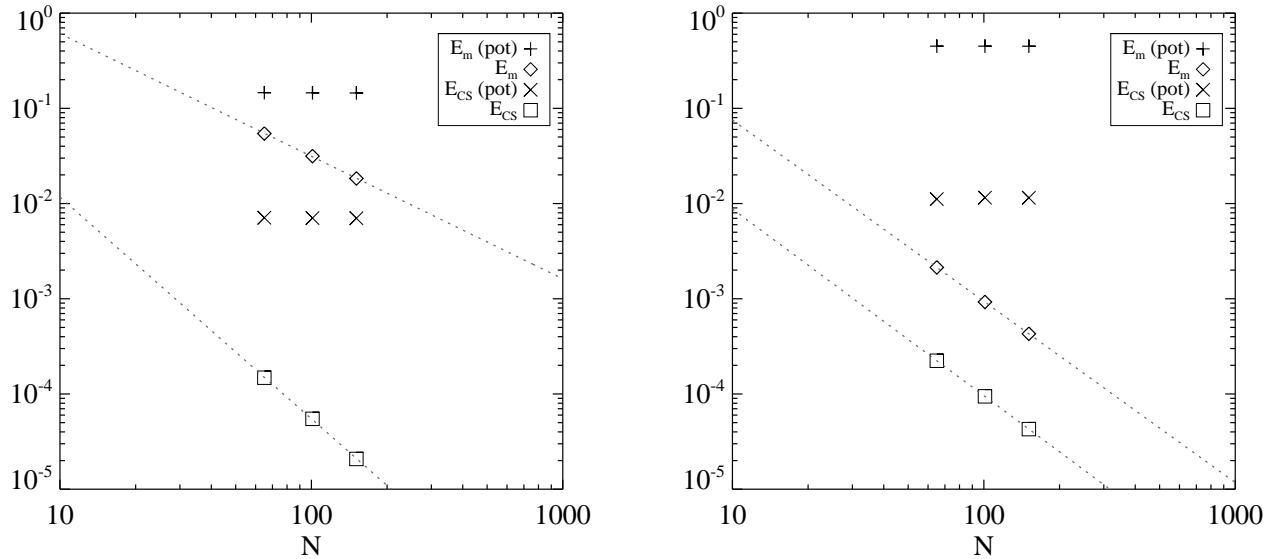


Figure 4. Error metrics E_m (see Equation (45)) and E_{CS} (see Equation (46)) as a function of grid size N for the initial potential field (plus signs and crosses), and for the numerical solution (diamonds and squares). The left panel shows the results for the test cases with periodic side boundary conditions after 30 Grad-Rubin iterations, and the right panel shows the results for the test cases with closed side boundary conditions after 50 Grad-Rubin iterations. The Grad-Rubin solutions show power-law scaling $E_m \sim N^\gamma$ and $E_{CS} \sim N^\gamma$, and the dashed lines show power-law fits to the data. The power-law indices γ for each fit are summarized in Table 1.

The left panel of Figure 4 shows E_m and E_{CS} for the initial potential field (plus signs and crosses), and for the numerical solution after 30 Grad-Rubin iterations (diamonds and squares), as functions of grid size N . The error associated with the potential field is independent of N . For the Grad-Rubin solution both E_m and E_{CS} decrease approximately as power laws, *i.e.* show scalings $\sim N^\gamma$, where we find (based on least squares fits) $\gamma = -1.3$ for E_m and $\gamma = -2.3$ for E_{CS} . The power-law fits are shown in Figure 4 by the dashed lines. The scaling for E_m is close to the expected $\sim 1/N$ scaling discussed in Section 3.2.2, while the scaling for E_{CS} is closer to $\sim 1/N^2$.

The left panel of Figure 5 shows E_{div} as a function of N for the numerical solution after 30 Grad-Rubin iterations (diamonds) and the analytic solution (plus signs). The two data sets overlap indicating that the divergence of the numerical solution is close to or smaller than the truncation error in the numerical derivative. In common with E_m and E_{CS} , the metric E_{div} for the Grad-Rubin solution has power-law scaling $\sim N^\gamma$. We estimate $\gamma = -2.0$ based on a least squares fit to the data for the Grad-Rubin solution (the power-law fit is shown as a dashed line in the figure).

We also measure the run time of the code for different grid sizes using the CPU clock (the tests are performed on an eight core CPU). Figure 6 shows the execution time for 30 Grad-Rubin iterations as a function of N . The results appear to follow a power law $\sim N^\gamma$, and we estimate $\gamma = 3.8$ based on a least squares fit to the three data points (the fit is shown by the dashed line). This scaling is close to the $\sim N^4$ scaling expected for the field line tracing discussed in Section 3.2.2. This scaling implies that the field line tracing is the computationally slowest step in the calculation.

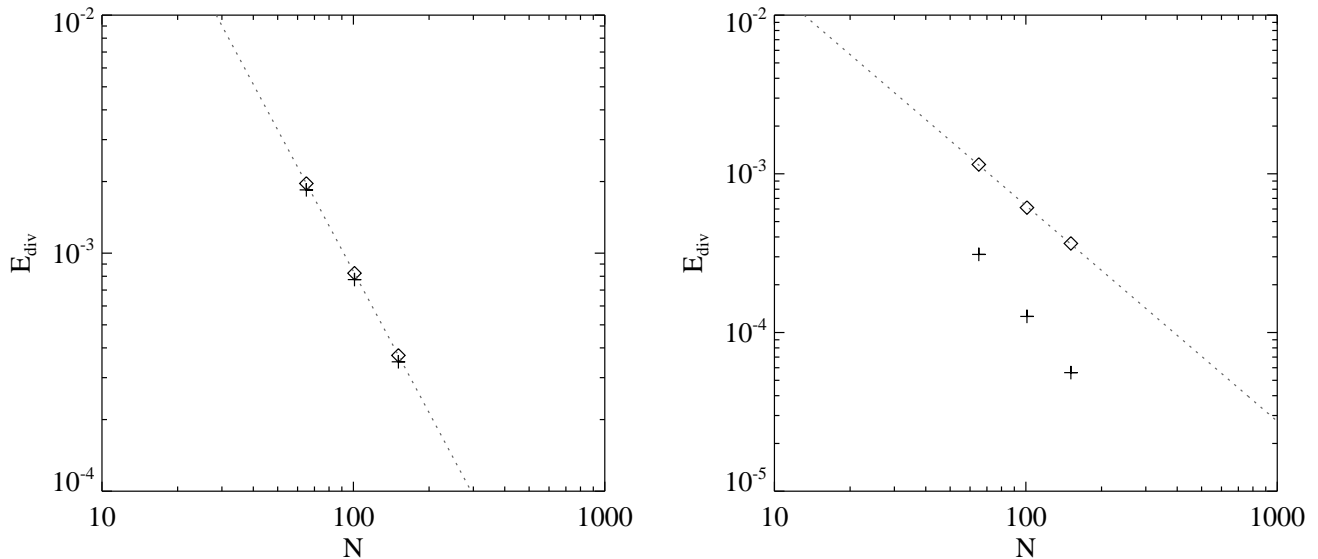


Figure 5. The absolute value of the divergence of the numerical solution and initial potential fields, averaged over the computational domain E_{div} (see Equation (47)) as a function of grid size N . The left panel shows E_{div} for the analytic solution (plus signs) and the numerical solution after 30 Grad-Rubin iterations for the test case with periodic boundary conditions. The right panel shows E_{div} for the analytic solution (plus signs) and the numerical solution after 50 Grad-Rubin iterations for the test case with closed boundary conditions. The dashed lines are power-law fits ($\sim N^\gamma$) to E_{div} for the numerical solutions. The power-law indices are $\gamma = -2.0$ for the data in the left panel, and $\gamma = -1.4$ for the data in the right panel. The power-law index for E_{div} for the analytic solutions in both panels is $\gamma = -2.0$. The fits are not shown.

5.2. Test Case with Closed Side Boundaries

For the second test we use the parameters $k = \pi/L$, $\lambda = 0.9\pi/L$, and $a_0 = 1$. The grid sizes are the same as in Section 5.1, and we apply 50 Grad-Rubin iterations starting from a potential field.

The right panel of Figure 2 shows ΔB_{avg} over 50 Grad-Rubin iterations for the three grid sizes used. For all three cases ΔB_{avg} decreases exponentially for roughly 40 iterations before becoming approximately constant. The rate of convergence does not appear to depend strongly on the grid size.

Figure 7 shows the field lines of the analytic solution, the potential field, and the Grad-Rubin solution. The view in the two panels in the figure is along the y axis. The left panel shows the field lines of the initial potential field (blue field lines) and of the analytic solution (red field lines). The right panel shows the field lines of the Grad-Rubin solution after 50 Grad-Rubin iterations (blue field lines) and of the analytic solution (red field lines). The Grad-Rubin solution closely matches the analytic solution.

The right panel of Figure 4 shows the error metrics E_m and E_{CS} for the initial potential field (plus signs and crosses), and for the numerical solution after 50 Grad-Rubin iterations (diamonds and squares). The error associated with the potential field is independent of N . For the Grad-Rubin solution both E_m and E_{CS} decrease as power-laws, with indices $\gamma = -1.9$ for E_m and $\gamma = -2.0$ for E_{CS} (based on least-squares fits, shown by the dashed lines). Both error metrics are found to scale approximately as $1/N^2$. The expected scaling, discussed in Section 3.2.2, is $\sim 1/N$. The improvement

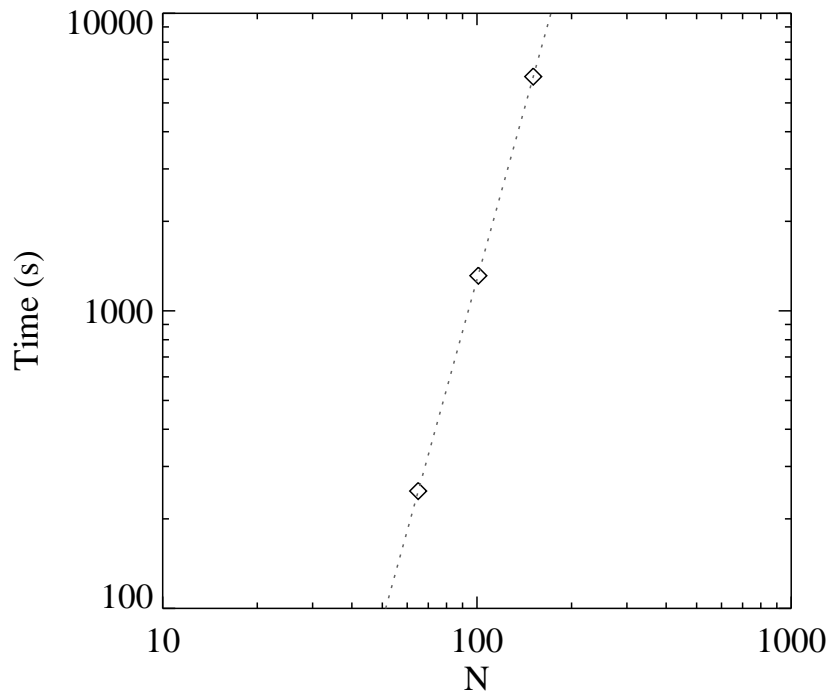


Figure 6. Execution time for 30 Grad-Rubin iterations as a function of grid size N for the first test case (Section 5.1). The execution time has power-law scaling with a power-law index $\gamma = 3.8$ based on a least-squares fit to the data (the dashed line).

in the observed scaling may be due to the simplicity of the solution (for this solution $B_y = 0$) and is unlikely to occur more generally.

The right panel of Figure 5 shows the error metric E_{div} as a function of N for the numerical solution after 50 Grad-Rubin iterations (diamonds) and for the analytic solution (plus signs). In this case E_{div} for the Grad-Rubin solution has power-law with index $\gamma = -1.0$ (based on a least squares fit to the data, shown as a dashed line in the figure). The analytic solution has a power-law scaling in E_{div} with $\gamma = -2.0$ (the fit is not shown). There is a substantial difference between E_{div} for the analytic and numerical solution indicating that E_{div} is providing a measure of the residual divergence of the numerical solution and is not due to the truncation error incurred by the numerical approximation to differentiation.

6. Discussion and Conclusion

We present an implementation of the Grad-Rubin method for solving the magnetostatic equations in a finite domain. The code allows two possible choices of boundary conditions on the side boundaries of the domain: either \mathbf{B} is periodic on the side boundaries, or the normal component of \mathbf{B} is zero on the side boundaries. We refer to these choices as periodic boundary conditions and closed boundary conditions. In both cases the normal component of \mathbf{B} is zero on the top boundary of the domain.

The code is tested in application to a simple analytic solution, for two choices of parameters for the solution, which illustrate the periodic and closed boundary conditions

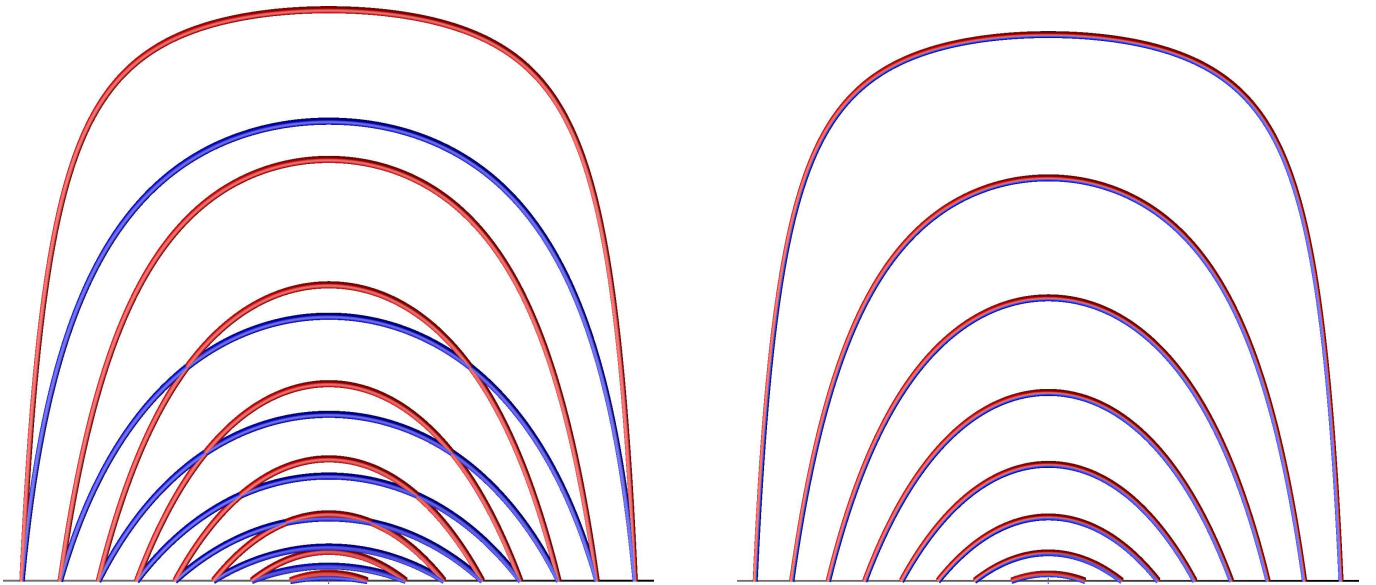


Figure 7. Comparison between the field lines for the analytic solution, the Grad-Rubin solution and the initial potential field for the test case in Section 5.2. The left panel shows the analytic solution (red field lines) and the potential field (blue field lines). The right panel shows the analytic solution (red field lines) and the numerical solution after 50 Grad-Rubin iterations (blue field lines). The view is along the y axis in both panels. The Grad-Rubin solution closely matches the analytic solution.

respectively. In both cases the code accurately reconstructs the test solution. Several runs are performed for each test case with varying grid sizes, to demonstrate the scaling of the method with the size of the problem. The test case is highly idealized. The lower boundary conditions are exactly consistent with the magnetostatic model because they are derived from an exact solution, and the top and side boundary conditions exactly match the assumptions adopted for the numerical method. The idealization allows a rigorous test of the correctness of the implementation.

For both test cases the Grad-Rubin method converges. The convergence is measured using the average absolute change ΔB_{avg} in the field (see Equation (44)). The test case with periodic boundary conditions converges faster than the test case with closed boundary conditions, measured in the number of iterations. This is likely due to the second test case being significantly more non-potential than the first, rather than being due to the different boundary conditions.

The code is found to accurately reproduce the analytic test cases. This is confirmed by a visual comparison of the field lines of the analytic solution and the reconstructed solution. For both choices of parameters/boundary conditions the numerical solution succeeds, based on this test. We also measure the success using the mean vector error E_m which is defined by Equation (45), and the Cauchy-Schwartz inequality based metric E_{CS} , which is defined by Equation (46). We also compute a measure of the residual divergence E_{div} which is defined by Equation (47). In the absence of numerical error we would expect $E_m = E_{\text{CS}} = E_{\text{div}} = 0$. For both test cases E_m , E_{CS} , and E_{div} decrease as N increases, with a power-law scaling in N , and we estimate the power-law index in each case from a least-squares fit to the data. The power-law indices are summarized in Table 1. We obtain different scalings for the different metrics in each case. This may be attributed to the difference between the two test cases, and the different metrics. The slowest scaling achieved is $\sim 1/N$ in each case, which is consistent with other Grad-Rubin implementations (Wheatland, 2006), and with the estimate made in Section

3.2.2. The fastest scaling achieved is $\sim 1/N^2$, which may be attributed to the simple form of the analytic solutions and is unlikely to be achieved for more general solutions. In general we expect a scaling $\sim 1/N$.

Table 1. Power law indices γ for the scaling of the error metrics E_m , E_{CS} , and E_{div} with grid size.

Test case	E_m	E_{CS}	E_{div}
Periodic	-1.3	-2.3	-2.0
Closed	-1.9	-2.0	-1.4

The execution time of the code is found to scale as $\sim N^4$, which is comparable to the fastest force-free Grad-Rubin methods (*e.g.* Wheatland 2006, 2007). However, the magnetostatic implementation is significantly slower in absolute terms than the force-free methods. The slowest step in both cases (force-free and magnetostatic) is the field line tracing used to update quantities in the volume at each iteration, and the magnetostatic case has two field line tracing steps (for $\sigma^{(k)}$ and $p^{(k)}$) compared to one (for $\alpha^{(k)}$) in the force-free case.

This paper demonstrates the new method and code in application to a simple test case. The long-term goal of our work is to develop a method and code for reconstructing coronal magnetic fields for real solar data. Several obstacles remain to be overcome before this can be achieved. One problem is observational: the photospheric pressure profile is not currently available for real solar cases. However, progress might be made by assuming a simple model for the pressure, *e.g.* a constant β model, with $p \propto |\mathbf{B}|^2$. Our model is also overly simplified in that we neglect gravity, and include only a pressure force. We are presently considering ways to include gravity also. Finally, it remains to be seen how well the techniques being developed cope with noisy data, and with data which are not strictly consistent with the magnetostatic model. Despite these qualifications, the method outlined here, and its successful application to analytic test cases, represents an important first step towards a Grad-Rubin method for magnetostatic reconstructions of the coronal magnetic field.

Appendix A

A potential field \mathbf{B}_0 satisfying

$$\nabla \times \mathbf{B}_0 = 0 \quad (48)$$

and the boundary conditions at $z = 0$

$$\mathbf{B}_0 \cdot \hat{\mathbf{z}} = B_{\text{obs}} \quad (49)$$

is used to initiate the Grad-Rubin iteration. The appropriate field with periodic side boundary conditions is given in Equation (24)-(26) in the text. For the choice of closed side boundaries the appropriate choice is

$$B_{0x}(x, y, z) = \sum_{m=0}^{\infty} \sum_{n=0}^{\infty} c_{mn} k_m \cosh(k[z - L]) \sin(k_m x) \cos(k_n y), \quad (50)$$

$$B_{0y}(x, y, z) = \sum_{m=0}^{\infty} \sum_{n=0}^{\infty} c_{mn} k_n \cosh(k[z - L]) \cos(k_m x) \sin(k_n y), \quad (51)$$

and

$$B_{0z}(x, y, z) = - \sum_{m=0}^{\infty} \sum_{n=0}^{\infty} c_{mn} k \sinh(k[z - L]) \cos(k_m x) \cos(k_n y), \quad (52)$$

where $k_m = \pi m/L$, $k_n = \pi n/L$, $k^2 = k_m^2 + k_n^2$, and where the coefficients c_{mn} are given by

$$c_{mn} = \frac{4}{L^2} \int_0^L \int_0^L dx dy B_{\text{obs}}(x, y) \cos(k_m x) \cos(k_n y) / \sinh(kL). \quad (53)$$

Equations (50)-(53) may be evaluated on a grid with N^3 points in $\sim N^3 \log(N)$ operations using fast sine and cosine transforms (Poularikas, 1996).

Appendix B

This appendix presents the solution for the current-carrying component of the test field, \mathbf{B}_c , with closed top and side boundary conditions. The magnetic field may be calculated from a vector potential \mathbf{A} in the Coulomb gauge ($\nabla \cdot \mathbf{A} = 0$) using $\nabla \times \mathbf{A} = \mathbf{B}_c$. The vector potential satisfies the vector Poisson equation (Jackson, 1998):

$$\nabla^2 \mathbf{A} = -\mu_0 \mathbf{J}. \quad (54)$$

The boundary conditions for \mathbf{B}_c on the six plane boundaries are

$$\mathbf{B}_c \cdot \hat{\mathbf{n}} = 0, \quad (55)$$

where $\hat{\mathbf{n}}$ is the unit vector normal to the boundary. The corresponding boundary conditions for the vector potential in the Coulomb gauge are (Amari, Boulmezaoud, and Mikić, 1999):

$$\partial_n \mathbf{A} = 0, \quad (56)$$

and

$$\mathbf{A}_t = 0, \quad (57)$$

where \mathbf{A}_t denotes the component of \mathbf{A} transverse to the boundary, and $\partial_n \mathbf{A}$ denotes the normal derivative.

The vector potential \mathbf{A} satisfying the boundary conditions Equations (56)-(57) can be written as a Fourier series:

$$A_x = \sum_{m=0}^{\infty} \sum_{n=0}^{\infty} \sum_{p=0}^{\infty} a_{mnp}^{(1)} \cos(k_m x) \sin(k_n y) \sin(k_p z), \quad (58)$$

$$A_y = \sum_{m=0}^{\infty} \sum_{n=0}^{\infty} \sum_{p=0}^{\infty} a_{mnp}^{(2)} \sin(k_m x) \cos(k_n y) \sin(k_p z), \quad (59)$$

and

$$A_z = \sum_{m=0}^{\infty} \sum_{n=0}^{\infty} \sum_{p=0}^{\infty} a_{mnp}^{(3)} \sin(k_m x) \sin(k_n y) \cos(k_p z), \quad (60)$$

where $k_m = \pi m/L$, $k_n = \pi n/L$, and $k_p = \pi p/L$. In the following we solve the Poisson equation to find an expression for a_{mnp} . The process is demonstrated for the A_x component, but the approach is similar for the other components.

Substituting Equation (58) into the Poisson equation (Equation (54)) gives

$$A_x = \sum_{m=0}^{\infty} \sum_{n=0}^{\infty} \sum_{p=0}^{\infty} a_{mnp}^{(1)} k^2 \cos(k_m x) \sin(k_n y) \sin(k_p z) = \mu_0 J_x(x, y, z), \quad (61)$$

where $k^2 = k_m^2 + k_n^2 + k_p^2$.

Applying the standard orthogonality relations (where δ_{mn} is the Kronecker delta):

$$\int_0^L \sin(\pi m s/L) \sin(\pi n s/L) ds = \frac{L}{2} \delta_{mn}, \quad (62)$$

$$\int_0^L \cos(\pi m s/L) \cos(\pi n s/L) ds = \frac{L}{2} \delta_{mn}, \quad (63)$$

and

$$\int_0^L \sin(\pi ms/L) \cos(\pi ns/L) ds = 0 \quad (64)$$

yields

$$a_{mnp}^{(1)} = \frac{8\mu_0}{L^3} \int_0^L \int_0^L \int_0^L J_x(x, y, z) \cos(k_m x) \sin(k_n y) \sin(k_p z) dx dy dz. \quad (65)$$

Similar expressions apply for the other two coefficients:

$$a_{mnp}^{(2)} = \frac{8\mu_0}{L^3} \int_0^L \int_0^L \int_0^L J_y(x, y, z) \sin(k_m x) \cos(k_n y) \sin(k_p z) dx dy dz, \quad (66)$$

and

$$a_{mnp}^{(3)} = \frac{8\mu_0}{L^3} \int_0^L \int_0^L \int_0^L J_z(x, y, z) \sin(k_m x) \sin(k_n y) \cos(k_p z) dx dy dz. \quad (67)$$

The magnetic field is obtained by evaluating $\mathbf{B}_c = \nabla \times \mathbf{A}$. The components of \mathbf{B}_c are

$$B_{cx}(x, y, z) = \sum_{m=0}^{\infty} \sum_{n=0}^{\infty} \sum_{p=0}^{\infty} [k_n a_{mnp}^{(3)} - k_p a_{mnp}^{(2)}] \sin(k_m x) \cos(k_n y) \cos(k_p z) / k^2, \quad (68)$$

$$B_{cy}(x, y, z) = \sum_{m=0}^{\infty} \sum_{n=0}^{\infty} \sum_{p=0}^{\infty} [k_p a_{mnp}^{(1)} - k_m a_{mnp}^{(3)}] \cos(k_m x) \sin(k_n y) \cos(k_p z) / k^2, \quad (69)$$

(70)

and

$$B_{cz}(x, y, z) = \sum_{m=0}^{\infty} \sum_{n=0}^{\infty} \sum_{p=0}^{\infty} [k_m a_{mnp}^{(2)} - k_n a_{mnp}^{(1)}] \cos(k_m x) \cos(k_n y) \sin(k_p z) / k^2. \quad (71)$$

The solution given by Equations (68)-(71) may be computed on a grid with N^3 points in $\sim N^3 \log(N)$ operations using a combination of fast sine and cosine transforms.

Acknowledgements S. A. Gilchrist acknowledges the support of an Australian Postgraduate Research Award.

References

- Aly, J.J., Amari, T.: 2007, *Geophys. Astrophys. Fluid Dyn.* **101**, 249.
- Alissandrakis, C.E.: 1981, *Astron. Astrophys.* **100**, 197.
- Amari, T., Boulmezaoud, T.Z., Mikic, Z.: 1999, *Astron. Astrophys.* **350**, 1051.
- Amari, T., Boulmezaoud, T.Z., Aly, J.J.: 2006, *Astron. Astrophys.* **446**, 691.
- Amari, T., Boulbe, C., Boulmezaoud, T.Z.: 2009, *SIAM J. Sci. Comput.* **31**, 3217.
- Barbosa, D.D.: 1978, *Solar Phys.* **56**, 55.
- Bineau, M.: 1972, *Comm. Pure Appl. Math.* **25**, 77.
- Boulmezaoud, T.Z., Amari, T.: 2000, *Z. Angew. Math. Phys.* **51**, 942.
- Chandra, R., Menon, R., Dagum, L., Kohr, D., Maydan, D., McDonald, J.: 2001, *Parallel Programming in OpenMP*, Morgan Kaufmann Publishers, San Francisco, 1.
- De Rosa, M.L., Schrijver, C.J., Barnes, G., Leka, K.D., Lites, B.W., Aschwanden, M.J., et al.: 2009, *Astrophys. J.* **696**, 1780.
- Fuhrmann, M., Seehafer, N., Valori, G.: 2007, *Astron. Astrophys.* **476**, 349.
- Gary, G.A.: 2001, *Solar Phys.* **203**, 71.
- Grad, H., Rubin, H.: 1958, *Proc. 2nd Int. Conf. Peaceful Uses of Atomic Energy*, **31**, 190.
- Hyder, C.L.: 1964, *Astrophys. J.* **140**, 817.
- Jackson, J.D.: 1998, *Classical Electrodynamics, 3rd edn.*, Wiley, New York, 180.
- Kaiser, R., Neudert, M., von Wahl, W.: 2000, *Commun. Math. Phys.* **211**, 111.
- Landi Degl'Innocenti, E., Landolfi, M.: 2004, *Polarization in Spectral Lines*, Kluwer Academic Publishers, Dordrecht, 625.
- Lin, H., Kuhn, J.R., Coulter, R.: 2004, *Astrophys. J. Lett.* **613**, 177.
- Metcalf, T.R., Jiao, L., McClymont, A.N., Canfield, R.C., Uitenbroek, H.: 1995, *Astrophys. J.* **439**, 474.
- Morse, P.M., Feshbach, H.: 1953, *Methods of Theoretical Physics, part two*, McGraw-Hill, New York, 1252.
- Nakagawa, Y., Raadu, M. A.: 1972, *Solar Phys.* **25**, 127.
- Poularikas, A.D.: 1996, In: Poularikas, A.D. (ed.), *The Transform and Applications Handbook*, CRC Press, Florida, 227.

-
- Press, W.H., Teukolsky, S.A., Vetterling, W.T., Flannery, B.P.: 1992, *Numerical Recipes in FORTRAN. The Art of Scientific Computing*, 2nd edn. Cambridge University Press, Cambridge, 181.
- Priest, E.R.: 1984, *Solar Magnetohydrodynamics*, D.Reidel Publishing Company, Dordrecht, 117.
- Reiman, A., Greenside, H.: 1986, *Comp. Phys. Com.* **43**, 157.
- Rudenko, G.V.: 2001, *Solar Phys.* **198**, 279.
- Sakurai, T.: 1989, *Space Sci. Rev.* **51**, 11.
- Schrijver, C.J., De Rosa, M.L., Metcalf, T.R., Barnes, G., Lites, B., Tarbell, T., *et al.*: 2008, *Astrophys. J.* **675**, 1637.
- Schrijver, C.J., De Rosa, M.L., Metcalf, T.R., Liu, Y., McTiernan, J., Régnier, S., Valori, G., Wheatland, M.S., Wiegelmann, T.: 2006, *Solar Phys.* **235**, 161.
- Seehafer, N.: 1978, *Solar Phys.* **58**, 215.
- Sturrock, P.A.: 1994, *Plasma Physics, An Introduction to the Theory of Astrophysical, Geophysical and Laboratory Plasmas*, Cambridge University Press, Cambridge, 206.
- Wiegelmann, T., Neukirch, T.: 2006, *Astron. Astrophys.* **457**, 1053.
- Wiegelmann, T., Neukirch, T., Ruan, P., Inhester, B.: 2007, *Astron. Astrophys.* **475**, 701.
- Wiegelmann, T.: 2008, *J.Geophys. Res. A* **113**, 3.
- Wiegelmann, T., Inhester, B., Sakurai, T.: 2006, *Solar Phys.* **233**, 215.
- Wiegelmann, T., Inhester, B.: 2003, *Solar Phys.* **214**, 287.
- Wiegelmann, T.: 1998, *Physica Scripta Volume T* **74**, 77.
- Wheatland, M.S.: 2006, *Solar Phys.* **238**, 29.
- Wheatland, M.S.: 2007, *Solar Phys.* **245**, 251.
- White, S.M., Kundu, M.R.: 1997, *Solar Phys.* **174**, 31.
- Zikanov, O: 2010, *Essential Computational Fluid Dynamics*, Wiley, New Jersey, 66.